

Short-range order and its impact on the CrCoNi medium-entropy alloy

<https://doi.org/10.1038/s41586-020-2275-z>

Received: 31 July 2019

Accepted: 9 March 2020

Published online: 20 May 2020

 Check for updates

Ruopeng Zhang^{1,2,5}, Shiteng Zhao^{1,2,5}, Jun Ding³, Yan Chong^{1,2}, Tao Jia⁴, Colin Ophus², Mark Asta^{1,3}, Robert O. Ritchie^{1,3} & Andrew M. Minor^{1,2}✉

Traditional metallic alloys are mixtures of elements in which the atoms of minority species tend to be distributed randomly if they are below their solubility limit, or to form secondary phases if they are above it. The concept of multiple-principal-element alloys has recently expanded this view, as these materials are single-phase solid solutions of generally equiatomic mixtures of metallic elements. This group of materials has received much interest owing to their enhanced mechanical properties^{1–5}. They are usually called medium-entropy alloys in ternary systems and high-entropy alloys in quaternary or quinary systems, alluding to their high degree of configurational entropy. However, the question has remained as to how random these solid solutions actually are, with the influence of short-range order being suggested in computational simulations but not seen experimentally^{6,7}. Here we report the observation, using energy-filtered transmission electron microscopy, of structural features attributable to short-range order in the CrCoNi medium-entropy alloy. Increasing amounts of such order give rise to both higher stacking-fault energy and hardness. These findings suggest that the degree of local ordering at the nanometre scale can be tailored through thermomechanical processing, providing a new avenue for tuning the mechanical properties of medium- and high-entropy alloys.

Among the increasing number of medium- to high-entropy alloy systems reported in the literature^{8–12}, the CrCoNi-based, face-centred-cubic (fcc) single-phase alloys exhibit an exceptional combination of mechanical properties, including high strength, tensile ductility, fracture toughness and impact resistance¹³. Extensive studies have documented the deformation mechanisms in these alloys. Gludovatz et al. reported the outstanding fracture toughness of CrCoNi at cryogenic temperatures¹⁴, and attributed this to a synergy of deformation mechanisms, including a propensity for mechanical twinning¹⁵. Interestingly, computational work has suggested that the CrCoNi-based fcc single-phase alloys should have near-zero or negative stacking-fault energies (SFEs; γ_{SF})^{15–19}. However, these computational predictions do not agree with measured values^{20,21} ($\gamma_{\text{SF, CrCoNi}} \approx 22 \text{ mJ m}^{-2}$ and $\gamma_{\text{SF, CrMnFeCoNi}} \approx 30 \text{ mJ m}^{-2}$). Experimentally, the measured SFEs in medium-entropy alloys (MEAs) and high-entropy alloys (HEAs) exhibit a wide distribution²², indicating a strong dependence of γ_{SF} on local atomic configuration. Ding et al.⁶ showed that the SFE of CrCoNi MEA can be tailored over a wide range by tuning its local chemical order. The work highlights the potentially strong impact of chemical short-range order (SRO) on the mechanical properties of the MEA/HEAs. Later, Li et al.⁷, using molecular dynamics simulations, demonstrated the ruggedness of the local energy landscape and how it raises activation barriers governing dislocation activities. Experimental evidence for the existence of such SRO has so far been limited to X-ray adsorption measurements²³ that are averaged over a relatively large volume of material. Indeed, further efforts are

needed to characterize the degree and the spatial extent of the ordering, as well as how both would be affected by thermal history and any associated effects on mechanical behaviour. Here we provide quantitative visualization of the SRO structure, by which we establish a direct effect of this SRO on the mechanical behaviour of MEA/HEA materials.

To investigate the presence of chemical SRO, samples of equiatomic CrCoNi alloys were subjected to different thermal treatments after homogenization at 1,200 °C: (1) water-quenched to room temperature to suppress SRO formation; or (2) aged at 1,000 °C for 120 h followed by slow furnace cooling to promote SRO formation. The microstructure and the degree of SRO were characterized with a variety of transmission electron microscope (TEM) imaging techniques. Diffraction contrast from SRO is inherently faint as compared to the fcc matrix lattice diffraction signal because the former arises from relatively minor differences in lattice distortion. As a result, measurement of the faint SRO diffraction signal has proven to be challenging. In order to enhance the signal-to-noise ratio of the diffraction contrast from SRO, we minimized the background noise from inelastic scattering by using a Zeiss TEM (LIBRA 200MC) equipped with an in-column Ω energy filter and a camera with 16-bit dynamic range. Energy-filtered diffraction patterns and dark-field images for the two heat treatment conditions are shown in Fig. 1. In the diffraction patterns (Fig. 1a, b), streaks along {111} directions between fcc Bragg spots are clearly observed in the aged sample. Dark-field imaging taken with the objective aperture positioned in the centre of the streaked region shown in Fig. 1b was used to image the

¹Department of Materials Science and Engineering, University of California, Berkeley, CA, USA. ²National Center for Electron Microscopy, Molecular Foundry, Lawrence Berkeley National Laboratory, Berkeley, CA, USA. ³Materials Sciences Division, Lawrence Berkeley National Laboratory, Berkeley, CA, USA. ⁴Department of Physics, Stanford University, Stanford, CA, USA.

⁵These authors contributed equally: Ruopeng Zhang, Shiteng Zhao. ✉e-mail: aminor@lbl.gov

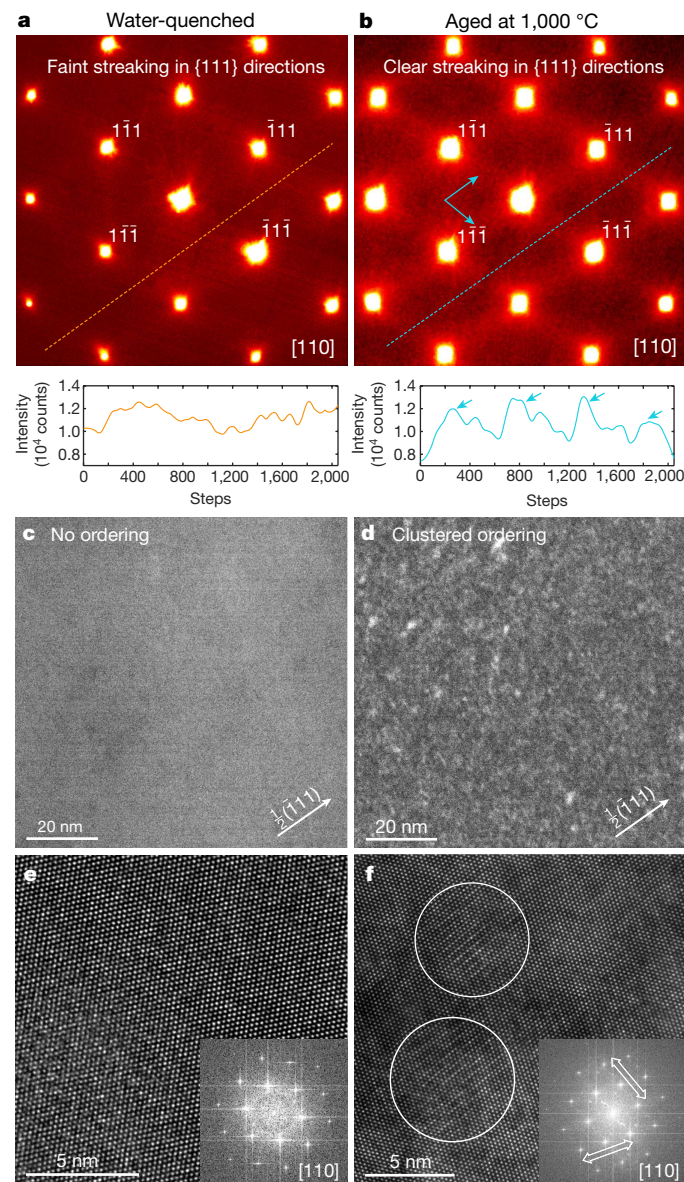


Fig. 1 | Energy-filtered TEM diffraction patterns, dark-field images formed with diffuse superlattice streaks and the associated high-resolution TEM images. Left column, water-quenched samples; right column, samples aged at 1,000 °C. **a, b,** Main panels, energy-filtered diffraction patterns for quenched and aged samples, respectively. The contrast is pseudo-coloured for better visibility. Plot below shows intensity measured along the diagonal line in the main panel; the periodic intensity of the diffuse superlattice streaks in **b** is marked by arrows. **c, d,** Energy-filtered dark-field images for quenched and aged samples, respectively. The aperture positions are marked by the **g** vectors (white arrows). **e, f,** Typical high-resolution TEM images of quenched and aged samples, respectively. Inset in each image is the associated FFT image. The features suggesting a superlattice are marked by the white circles, and the associated streaking along the $\{111\}$ directions is marked by the white arrows in the FFT image.

SRO domains directly. While no dark-field contrast can be seen from the water-quenched samples (Fig. 1c), the aged sample (Fig. 1d) clearly reveals nanoscale domains. Results from an intermediate heat treatment are shown in Extended Data Fig. 1 for comparison.

The diffuse scattering in the diffraction patterns and the associated contrast in the dark-field images could arise from a combination of effects, including static and thermal displacement scattering and chemical SRO²⁴. In the CrCoNi system, the very close values of atomic

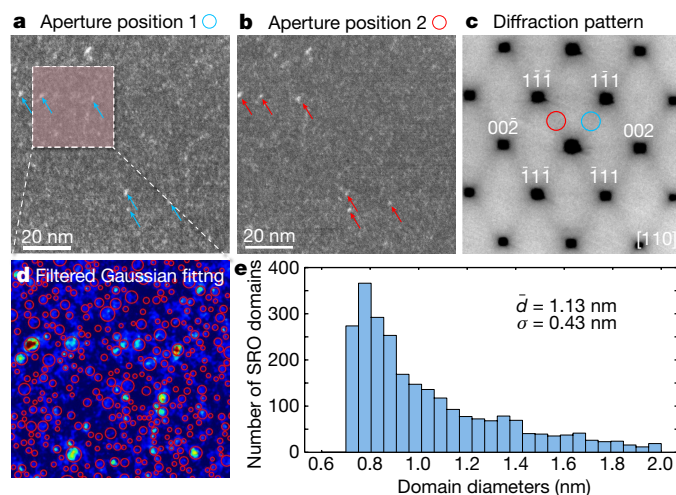


Fig. 2 | Evidence for the three-dimensional structure of the domains and their size distribution. **a, b,** Energy-filtered dark-field images from different diffuse superlattice peaks; examples showing the same domain contrast are marked with the arrows. **c,** Energy-filtered diffraction patterns of the region of interest; the red and blue circles indicate the dark-field imaging conditions of **a** and **b**. The contrast is reversed for better visibility. **d,** Magnified view of the boxed part of the dark-field image in **a**, with identified SRO domains marked by the red circles. The dark-field image is pseudo-coloured for better visibility. **e,** The histogram of identified domain diameters. The average value \bar{d} and the standard deviation σ are listed in the box.

scattering factors of the three elements would limit the contrast from any superlattice diffraction. However, the fact that the water-quenched samples (Fig. 1c) show negligible contrast using the same imaging conditions, and the fact that the aged samples show enhanced streaking and dark-field contrast, strongly support the interpretation that these features arise from the distortion of the local lattice associated with the formation of a diffuse SRO superlattice. Specifically, the enhanced contrast in samples aged at higher temperature and slow-cooled can be interpreted to be associated with the higher mobility of the atoms at these temperatures; this higher mobility enables the alloy to evolve towards a lower free-energy state with higher chemical SRO. Further evidence in support of this interpretation follows.

High-resolution TEM imaging (HRTEM) has been used to distinguish the difference between diffuse scattering induced by thermal displacement as compared to that induced by static displacement in previous studies²⁴. Figure 1e, f shows a comparison of HRTEM images from water-quenched and aged samples, where two regions in the aged sample show diffuse superlattice features along $\{111\}$ planes as marked in Fig. 1f. In addition, the two-dimensional fast Fourier transforms (FFTs) of the HRTEM images (Fig. 1e, f insets) show a similar streaking intensity along the reciprocal lattice vectors that are normal to the $\{111\}$ planes of the crystal. These observations provide clear evidence that the contrast in the real-space HRTEM images is associated directly with the diffuse intensity observed in the diffraction patterns. The features observed in the HRTEM images are qualitatively consistent with the type of order suggested in EXAFS²³ and in previous Monte Carlo simulations^{6,25}, both of which indicate that Cr–Cr pairs are strongly disfavoured at nearest-neighbour distances. Such bonding preferences are consistent with the alternating contrast caused by lattice distortion in the SRO domains along the $\langle 111 \rangle$ directions observed by HRTEM.

The combined conclusion from diffraction contrast and HRTEM imaging is that the high-temperature ageing leads to the formation of appreciable SRO in CrCoNi MEAs. The size and shape of the SRO-enhanced domains can thus be evaluated through energy-filtered dark-field imaging. For example, Fig. 2a, b presents two dark-field

images formed by using two different objective aperture positions as marked in Fig. 2c. While each dark-field image (Fig. 2a, b) shows mostly different sets of SRO-enhanced domains that are preferentially scattering to different parts of reciprocal space, there are a number of domains that could be identified in both images (examples are marked by the arrows). The existence of the same domains in images formed by separate and non-parallel directions of SRO-generated streaking is evidence for a non-planar shape of the SRO domains.

It is also possible to characterize the size distribution of the domains by assuming a shape (in this case we assume a spherical shape for simplicity) and applying a Gaussian template fitting algorithm²⁶ as demonstrated in the Methods section. This analysis generates an average diameter of the measured domains of 1.13 ± 0.43 nm, which would correspond to the third to fourth atomic shells on the fcc lattice of CrCoNi MEA^{17,20,27}. However, as the dark-field images in Figs. 1 and 2 suggest, the domain boundaries are relatively diffuse, and there is no evidence of any specific shape that characterizes the SRO domains. Further evidence for the diffuse nature of the SRO domains can be obtained by conducting geometrical phase analysis (GPA) on drift-corrected high-resolution scanning transmission electron microscope (STEM) images²⁸. The resulting strain maps are summarized in Extended Data Fig. 2. In the water-quenched sample, the fluctuation of local strain is minimal. However, in the sample aged at 1,000 °C, domain contrast similar in size to that found in the dark-field images could be identified, indicating small yet locally ordered fluctuations in lattice distortions. The results suggest that the SRO may be associated with the changes in the static atomic displacements, which is of interest since lattice distortions are widely proposed to partially explain the mechanical properties of the CrCoNi MEA¹³. This result thus warrants further investigation. We note, however, that standard X-ray diffraction (XRD) experiments conducted on both water-quenched and 1,000 °C aged samples show no evident changes in peak broadening for the two different thermal treatments (Extended Data Fig. 3), such that further investigations of the lattice distortions would probably require synchrotron measurements and lie beyond the scope of the present study.

It is known that the formation of SRO has a strong impact on dislocation plasticity—an increasing degree of SRO tends to increase the planarity of dislocation slip^{29–31}. To assess the effect in the CrCoNi alloy, dislocation analysis was conducted on bulk compressed samples and the results are summarized in Fig. 3. Specifically, a random distribution of dislocations was observed in the water-quenched sample, whereas a marked trend of localized planar configuration of dislocations was present in the 1,000 °C aged sample with SRO (Fig. 3a, b). In the latter case, the leading dislocations also tend to form dislocation pairs, where the separation distance of two adjacent dislocations was reduced (two examples are marked by the white arrows in Fig. 3b). One possible origin of planar slip in fcc materials is the Shockley partial dissociation of perfect dislocation cores, limiting the ability of dislocations to cross slip owing to the expanded cores. In the current study, however, the aged alloy possesses dislocation cores that are more compact than the quenched alloy while presenting planar slip. On the other hand, localized planar slip and leading dislocation pairs are usually correlated to the glide plane softening effect due to the local destruction of the SRO structure^{29,31,32}, where the initial dislocation motion interrupts the SRO atomic configuration and overcomes the energy barrier associated with the creation of a diffuse-anti-phase boundary (DAPB). Subsequently, dislocations following the initial dislocation would experience a lower energy barrier by gliding on the same path and avoiding the DAPB energy barrier. The DAPB energy as a function of dislocation slip events has been assessed by density functional theory (DFT) calculations based on the calculated SRO atomic configuration⁶, supporting this theory of the origin of the planar dislocation slip (Extended Data Fig. 4).

The exceptional strength, ductility and toughness of CrCoNi MEA can be directly correlated with the SFE of the material¹³. Previous DFT-assisted Monte Carlo simulations predicted that the SFE of CrCoNi

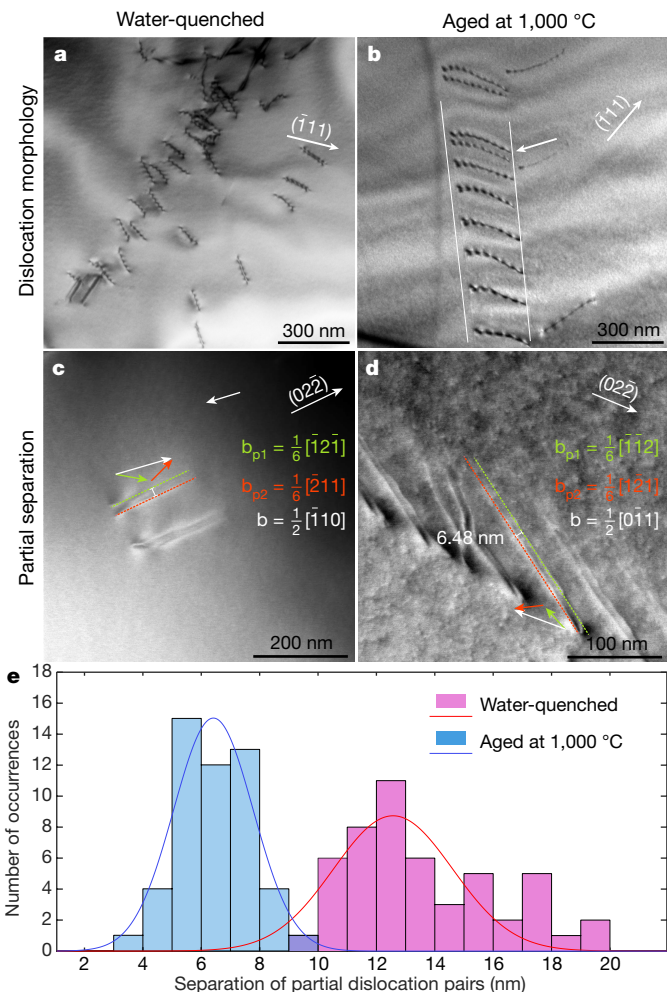


Fig. 3 | Dislocation analysis of both water-quenched and 1,000 °C aged samples. **a**, Two-beam bright-field image, showing the representative wavy configuration of dislocations in the water-quenched sample. The white arrow with the \mathbf{g} vector marks the two-beam diffraction condition utilized. **b**, Two-beam bright-field image, showing the representative planar configuration (marked by the parallel white lines) of dislocations in the 1,000 °C aged sample. The leading dislocation pair is marked by the white arrow. The white arrow with the \mathbf{g} vector marks the two-beam condition utilized. **c, d**, Low angle annular dark field (LAADF) images showing dislocation dissociations in water-quenched and 1,000 °C aged samples, respectively. The white arrows with the \mathbf{g} vectors mark the two-beam diffraction conditions utilized. The Burgers vector relations are demonstrated: green arrows, \mathbf{b}_{p1} ; red arrows, \mathbf{b}_{p2} ; white arrows, \mathbf{b} . The detailed ‘ $\mathbf{g}\cdot\mathbf{b}$ ’ analysis is summarized in Extended Data Fig. 5. Examples of measured partial dislocation separations are marked as 12.74 nm in **c** and 6.48 nm in **d**. **e**, Distribution of the measured separation of partial dislocation pairs from both water-quenched and 1,000 °C aged samples. The results of numerical analysis are summarized in Extended Data Table 1.

MEA could be highly tunable by varying the SRO⁶. While the SFE of MEA/HEAs has been experimentally probed previously via both weak-beam dark-field imaging²⁰ and diffraction contrast STEM (DC-STEM) analysis²², the SFE has never been directly correlated with the degree of SRO. In the current study, the SFE was measured by DC-STEM analysis as the technique allows imaging through thicker samples to minimize the sample surface effect. Figure 3c, d shows examples of images where partial dislocations could be identified and their disassociation measured directly (analysis detailed in Extended Data Fig. 5). The separation distance and the statistical results are summarized in Fig. 3e and Extended Data Table 1. The detailed calculation of the SFE is elaborated

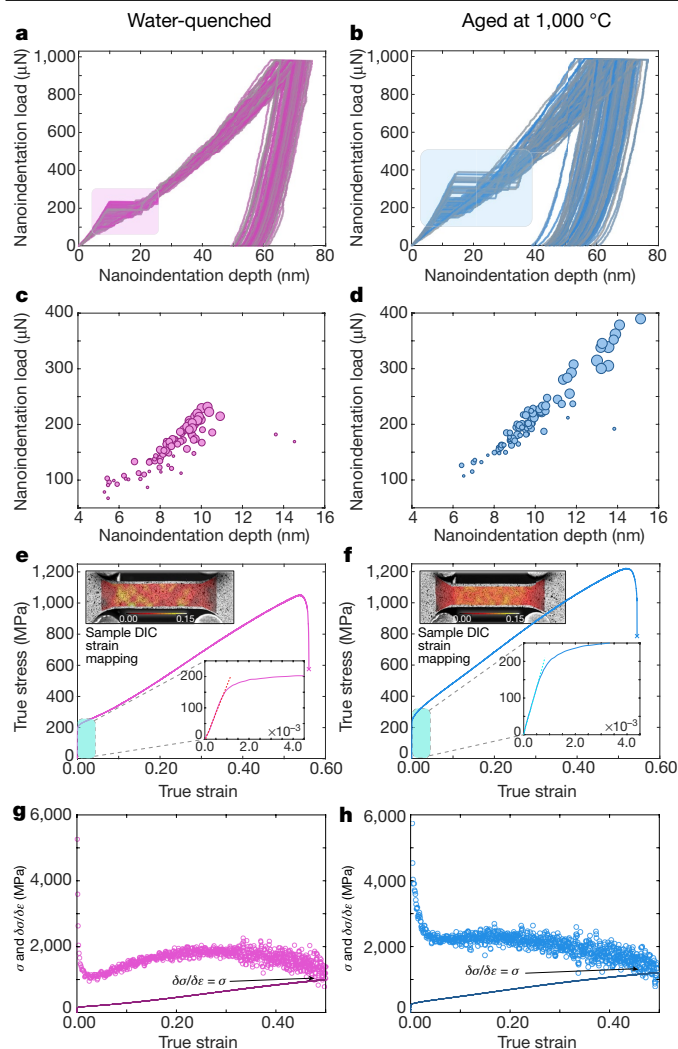


Fig. 4 | Comparison of mechanical properties from nanoindentation and bulk tensile tests. Left column, water-quenched samples; right column, samples aged at 1,000 °C. **a, b**, Load–depth curves from a 10×10 grid of nanoindentations separated by $10 \mu\text{m}$ from each other, from a water-quenched sample and a 1,000 °C aged sample, respectively. Pop-in analysis from these same tests are provided for water-quenched (**c**) and 1,000 °C aged (**d**) samples. Data points (circles) depict the depth and load when the pop-in events occur; the sizes of the circles are proportional to the total pop-in displacement. **e, f**, Results of tensile tests on a water-quenched sample and a 1,000 °C aged sample, respectively. Lower insets, the elastic portions of the curves (note that the inset x axis shows true strain $\times 10^{-3}$); upper insets, a sample image of the strain distribution during elastic loading, as determined by digital image correlation (DIC). **g, h**, Work hardening rate derived from the true stress–strain curves (σ , true stress; ε , true strain; $\delta\sigma/\delta\varepsilon$, calculated work hardening rate) of the water-quenched and the 1,000 °C aged samples, respectively. True stress versus true strain data from the same tests, respectively, are also displayed in **g, h** as the solid lines for comparison. The necking points ($\delta\sigma/\delta\varepsilon = \sigma$) are marked by the black arrows. The results of numerical analysis from these tests are summarized in Extended Data Table 1.

in the Methods section, and shows that the 1,000 °C aged samples have an SFE of $23.33 \pm 4.31 \text{ mJ m}^{-2}$, double the value of its water-quenched counterpart ($8.18 \pm 1.43 \text{ mJ m}^{-2}$). This measurement confirms that the SRO directly impacts the SFE, and indicates that the SFE could be fine-tuned by controlling the ordering⁶.

In order to quantify the impact of SRO on the mechanical properties of the CrCoNi MEA, both nanoindentation tests and bulk tensile tests were performed. The measured nanoindentation hardness is

$4.07 \pm 0.23 \text{ GPa}$ for the water-quenched sample and $4.37 \pm 0.58 \text{ GPa}$ for the 1,000 °C aged sample. SRO also significantly affects the onset of plasticity, which is manifested by the ‘pop-in’ event³³ in the load versus displacement curves in Fig. 4c, d. The first pop-in events of the 1,000 °C aged sample are distributed more discretely and usually occur at higher load than the quenched sample. In addition, the displacement plateau that corresponds to the strain burst of a pop-in event is larger in the aged material, as detailed in Extended Data Fig. 6. The higher pop-in load and larger displacement plateau in the 1,000 °C aged specimen indicates the presence of dislocation avalanches (sudden bursts of dislocation nucleation and propagation), providing further evidence of the SRO hardening and the subsequent glide plane softening caused by passage of the first few dislocations in the slip band. Bulk tensile tests confirmed the strengthening effect of SRO by showing an approximately 25% increase of the yield strength (Extended Data Table 1) as well as a marked change of the work hardening behaviour.

As demonstrated in Fig. 4g, h, the initial work hardening rate of the aged sample is twice that of its water-quenched counterpart, reinforcing the that the hardening is caused by the SRO domains. Traditionally, the formation of SRO in alloys causes planar dislocation slip and deformation localization^{29,34–36}. In some cases, the deformation localization affects the alloys’ ductility and toughness, whereas in the current study, the formation of SRO has little effect on the overall ductility of the MEA alloy. Deformation twinning is reported to explain the exceptional ductility of the CrCoNi alloy^{13,15}, in which nano-twinning delays deformation localization. Though direct evidence is lacking, when we consider the similar work-hardening behaviour at later stages of deformation of both the 1,000 °C aged and the water-quenched samples, we speculate that the exceptional strength and toughness of CrCoNi MEA arises in part from this unique combination of SRO hardening and twin-induced deformation at later stages. However, further systematic analysis is required to fully understand any potential effect of SRO on the deformation twinning.

As an emerging class of structural materials, MEA/HEAs possess a desirable combination of mechanical properties for structural applications^{13,37,38}. Although the concept of MEA/HEAs is based on production of a single-phase solid solution, there has long been a question about how well-mixed the solid solutions are^{4,8,13,23,39–43}. Here we directly imaged the local ordering and showed how the deformation behaviour of MEAs is directly correlated with the degree of SRO. Annealing the MEA to promote SRO led to an increase in hardness, a doubling of the SFE and a subsequent increase in planar slip. Owing to its impact on the mechanical properties, the degree of SRO is a critical feature that should be considered in the materials’ design phase. Directly tailoring the SRO microstructure on an atomic level therefore provides another route for controlling the structure–property relationship of advanced materials.

Online content

Any methods, additional references, Nature Research reporting summaries, source data, extended data, supplementary information, acknowledgements, peer review information; details of author contributions and competing interests; and statements of data and code availability are available at <https://doi.org/10.1038/s41586-020-2275-z>.

1. Yeh, J. W. et al. Nanostructured high-entropy alloys with multiple principal elements: novel alloy design concepts and outcomes. *Adv. Eng. Mater.* **6**, 299–303 (2004).
2. Cantor, B., Chang, I. T. H., Knight, P. & Vincent, A. J. B. Microstructural development in equiatomic multicomponent alloys. *Mater. Sci. Eng. A* **375–377**, 213–218 (2004).
3. Li, Z., Pradeep, K. G., Deng, Y., Raabe, D. & Tasan, C. C. Metastable high-entropy dual-phase alloys overcome the strength–ductility trade-off. *Nature* **534**, 227–230 (2016).
4. Gludovatz, B. et al. A fracture-resistant high-entropy alloy for cryogenic applications. *Science* **345**, 1153–1158 (2014).
5. Yang, T. et al. Multicomponent intermetallic nanoparticles and superb mechanical behaviors of complex alloys. *Science* **362**, 933–937 (2018).
6. Ding, J., Yu, Q., Asta, M. & Ritchie, R. O. Tunable stacking fault energies by tailoring local chemical order in CrCoNi medium-entropy alloys. *Proc. Natl Acad. Sci. USA* **115**, 8919–8924 (2018).

7. Li, Q.-J., Sheng, H. & Ma, E. Strengthening in multi-principal element alloys with local-chemical-order roughened dislocation pathways. *Nat. Commun.* **10**, 3563 (2019).
8. Zhang, Y. et al. Microstructures and properties of high-entropy alloys. *Prog. Mater. Sci.* **61**, 1–93 (2014).
9. Gao, M. C., Yeh, J. W., Liaw, P. K. & Zhang, Y. *High-Entropy Alloys: Fundamentals and Applications* (Springer International, 2016).
10. Senkov, O. N., Miracle, D. B., Chaput, K. J. & Couzinie, J. P. Development and exploration of refractory high entropy alloys — a review. *J. Mater. Res.* **33**, 3092–3128 (2018).
11. Miracle, D. B. High entropy alloys as a bold step forward in alloy development. *Nat. Commun.* **10**, 1805 (2019).
12. George, E. P., Raabe, D. & Ritchie, R. O. High-entropy alloys. *Nat. Rev. Mater.* **4**, 515–534 (2019).
13. Li, Z., Zhao, S., Ritchie, R. O. & Meyers, M. A. Mechanical properties of high-entropy alloys with emphasis on face-centered cubic alloys. *Prog. Mater. Sci.* **102**, 296–345 (2019).
14. Gludovatz, B. et al. Exceptional damage-tolerance of a medium-entropy alloy CrCoNi at cryogenic temperatures. *Nat. Commun.* **7**, 10602 (2016).
15. Zhang, Z. et al. Dislocation mechanisms and 3D twin architectures generate exceptional strength-ductility-toughness combination in CrCoNi medium-entropy alloy. *Nat. Commun.* **8**, 14390 (2017).
16. Zaddach, A. J., Niu, C., Koch, C. C. & Irving, D. L. Mechanical properties and stacking fault energies of NiFeCrCoMn high-entropy alloy. *J. Miner. Met. Mater. Soc.* **65**, 1780–1789 (2013).
17. Zhang, Y. H., Zhuang, Y., Hu, A., Kai, J. J. & Liu, C. T. The origin of negative stacking fault energies and nano-twin formation in face-centered cubic high entropy alloys. *Scr. Mater.* **130**, 96–99 (2017).
18. Zhao, S., Stocks, G. M. & Zhang, Y. Stacking fault energies of face-centered cubic concentrated solid solution alloys. *Acta Mater.* **134**, 334–345 (2017).
19. Niu, C., LaRosa, C. R., Miao, J., Mills, M. J. & Ghazisaeidi, M. Magnetically-driven phase transformation strengthening in high entropy alloys. *Nat. Commun.* **9**, 1363 (2018).
20. Laplanche, G. et al. Reasons for the superior mechanical properties of medium-entropy CrCoNi compared to high-entropy CrMnFeCoNi. *Acta Mater.* **128**, 292–303 (2017).
21. Okamoto, N. L. et al. Size effect, critical resolved shear stress, stacking fault energy, and solid solution strengthening in the CrMnFeCoNi high-entropy alloy. *Sci. Rep.* **6**, 35863 (2016).
22. Smith, T. M. et al. Atomic-scale characterization and modeling of 60° dislocations in a high-entropy alloy. *Acta Mater.* **110**, 352–363 (2016).
23. Zhang, F. X. et al. Local structure and short-range order in a NiCoCr solid solution alloy. *Phys. Rev. Lett.* **118**, 205501 (2017).
24. Van Tendeloo, G. & Amelinckx, S. The origin of diffuse intensity in electron diffraction patterns. *Phase Transit.* **67**, 101–135 (1998).
25. Tamm, A., Aabloo, A., Klintonberg, M., Stocks, M. & Caro, A. Atomic-scale properties of Ni-based FCC ternary, and quaternary alloys. *Acta Mater.* **99**, 307–312 (2015).
26. Zhang, R. et al. Direct imaging of short-range order and its relationship to deformation in Ti-6Al. *Sci. Adv.* **5**, eaax2799 (2019).
27. Laplanche, G. et al. Elastic moduli and thermal expansion coefficients of medium-entropy subsystems of the CrMnFeCoNi high-entropy alloy. *J. Alloys Compd.* **746**, 244–255 (2018).
28. Ophus, C., Ciston, J. & Nelson, C. T. Correcting nonlinear drift distortion of scanning probe and scanning transmission electron microscopies from image pairs with orthogonal scan directions. *Ultramicroscopy* **162**, 1–9 (2016).
29. Gerold, V. & Karthaler, H. P. On the origin of planar slip in f.c.c. alloys. *Acta Metall.* **37**, 2177–2183 (1989).
30. Pekin, T. C., Gammer, C., Ciston, J., Ophus, C. & Minor, A. M. In situ nanobeam electron diffraction strain mapping of planar slip in stainless steel. *Scr. Mater.* **146**, 87–90 (2018).
31. Neeraj, T. & Mills, M. J. Short-range order (SRO) and its effect on the primary creep behavior of a Ti-6wt.%Al alloy. *Mater. Sci. Eng. A* **319–321**, 415–419 (2001).
32. van de Walle, A. & Asta, M. First-principles investigation of perfect and diffuse antiphase boundaries in HCP-based Ti-Al alloys. *Metall. Mater. Trans. A* **33**, 735–741 (2002).
33. Gouldstone, A. et al. Indentation across size scales and disciplines: recent developments in experimentation and modeling. *Acta Mater.* **55**, 4015–4039 (2007).
34. Fisher, J. C. C. On the strength of solid solution alloys. *Acta Metall.* **2**, 9–10 (1954).
35. Britton, T. B., Dunne, F. P. E. & Wilkinson, A. J. On the mechanistic basis of deformation at the microscale in hexagonal close-packed metals. *Proc. R. Soc. A* **471**, 20140881 (2015).
36. Hamdi, F. & Asgari, S. Influence of stacking fault energy and short-range ordering on dynamic recovery and work hardening behavior of copper alloys. *Scr. Mater.* **62**, 693–696 (2010).
37. Miracle, D. B. et al. Exploration and development of high entropy alloys for structural applications. *Entropy* **16**, 494–525 (2014).
38. Williams, J. C. & Starke, E. A. Progress in structural materials for aerospace systems. *Acta Mater.* **51**, 5775–5799 (2003).
39. Ma, Y. et al. Chemical short-range orders and the induced structural transition in high-entropy alloys. *Scr. Mater.* **144**, 64–68 (2018).
40. Singh, P., Smirnov, A. V. & Johnson, D. D. Atomic short-range order and incipient long-range order in high-entropy alloys. *Phys. Rev. B* **91**, 224204 (2015).
41. Lucas, M. S. et al. Absence of long-range chemical ordering in equimolar FeCoCrNi. *Appl. Phys. Lett.* **100**, 251907 (2012).
42. Niu, C. et al. Spin-driven ordering of Cr in the equiatomic high entropy alloy NiFeCrCo. *Appl. Phys. Lett.* **106**, 161906 (2015).
43. Linden, Y., Pinkas, M., Munitz, A. & Meshi, L. Long-period antiphase domains and short-range order in a B2 matrix of the AlCoCrFeNi high-entropy alloy. *Scr. Mater.* **139**, 49–52 (2017).

Publisher's note Springer Nature remains neutral with regard to jurisdictional claims in published maps and institutional affiliations.

© This is a U.S. government work and not under copyright protection in the U.S.; foreign copyright protection may apply 2020

Methods

Materials and sample preparation

The raw ingot of the equiatomic CrCoNi MEA was argon-arc double melted and then cut into smaller samples. The samples were then divided into two groups and underwent different thermal treatments: (1) homogenized at 1,200 °C for 48 h then water quenched to room temperature (uniform texture, grain size ~800 μm as determined by electron backscatter diffraction, EBSD); or (2) homogenized at 1,200 °C for 48 h then aged at 1,000 °C for 120 h followed by furnace cooling (uniform texture, grain size ~1,000 μm as determined by EBSD). All the alloys were confirmed to be a single-phase fcc structure via X-ray diffraction and EBSD analysis. Samples for dislocation analysis were further deformed by conducting bulk compression tests on an MTS Criterion (Model 43) system to introduce dislocation plasticity. The final strain was 6% with a strain rate of 1×10^{-3} . The samples were then sliced and thinned by mechanical polishing. Electron-transparent samples for TEM observation were prepared with a Fischione twin-jet electropolisher using a solution of 70% methanol, 20% glycerol and 10% perchloric acid at -20 °C. The samples for nanoindentation tests were prepared by single-side electrochemical polishing with the aforementioned solution and parameters.

Energy-filtered TEM and SRO recognition

TEM samples of different heat treatments were used for observation. A Zeiss LIBRA 200MC microscope, equipped with an in-column Ω energy filter, was used to take both diffraction patterns and dark-field images. It is necessary to consider the impact of the objective aperture on the resolution, which could be estimated by the Airy disk radius using the following equation⁴⁴:

$$r_{\text{Airy}} \approx \frac{1.2\lambda f}{D} \quad (1)$$

where λ is the electron wavelength (0.02507 Å for 200 kV TEM), f is the focal length of the objective lens (~3 mm for the Zeiss LIBRA) and D is the diameter of the objective aperture (25 μm in the current study). For the experimental setup used in the current study, the size of the aperture Airy disk is 3.61 Å, which is below the size of the observed SRO domains. An alternative way to determine the resolution limit is to directly measure the semi-angle of the aperture used:

$$r_{\text{Airy}} \approx \frac{1.2\lambda}{\alpha} = 1.2d' \quad (2)$$

where α is the measured semi-angle of the aperture and d' is the measured size of the aperture in reciprocal space. This method yields a similar resolution limit of 3.03 Å, confirming sufficient resolution to resolve the SRO domains. A 5-eV energy slit was deployed to select the zero-loss peak and eliminate the contrast from inelastic scattering. A Gatan US1000 CCD camera was used to acquire the diffraction patterns and dark-field images. Before the data analysis, the energy-filtered dark-field images were filtered by a dark reference subtraction. According to the energy-filtered dark-field image shown in Figs. 1 and 2, there is no observable directional tendency of the domains. Therefore, we assumed a circular kernel signal from the domains for our analysis. SRO-enhanced domains were identified and measured through Gaussian template fitting, where 2D convolutions with the dark-field image were conducted using a list of differently sized 2D Gaussian templates (with different values of standard deviation²⁶). The stack of result images was further analysed through a circular Hough transform to identify all signal peaks. The intensity cutoff was set according to the best fit result. Overlapping entities were deleted to ensure an accurate size measurement. Details of the algorithm are given in Extended Data Table 2.

A manual sampling was carried out to estimate the domain sizes and gain a reference for the optimization of parameters. Two critical

parameters that would impact the identification are the minimal signal cutoff and the domain diameter range. The optimization process was conducted according to the best fitting results. In the case of a high signal cutoff or a narrow diameter range, the algorithm will miss some of the major contrast, whereas, in the case of a low signal cutoff or a wide diameter range, the algorithm will pick up many small intensity fluctuations that are from camera noise. It is worth mentioning the limitations to the domain recognition algorithm. Specifically, the assumption that the domains are spherical is for simplification, but the shapes of the domains vary. Parallel attempts using a threshold segmentation algorithm involved much more subjectivity and yielded unreasonable results. However, the purpose of the analysis is to provide an estimated size distribution of the SRO domains, for which the current analysis is sufficient until large-scale atomic imaging studies can provide similar statistics.

X-ray diffraction (XRD) experiments

The XRD experiments were performed *ex situ* with a PANalytical XPert diffractometer on water-quenched and on 1,000 °C aged samples. The scan range (2θ) was set to 42°–54° to include the (111) and the (200) peaks. The angle resolution was set to 0.005° with a 0.8-s integration time to ensure an accurate measurement of the lattice constants.

High-resolution STEM (HRSTEM) imaging

HRSTEM imaging of water-quenched and 1,000 °C aged samples were conducted on the double-corrected TEAM I microscope (operated at 300 kV) at the National Center for Electron Microscopy (NCEM), Lawrence Berkeley National Laboratory. Drift correction was conducted with the methods developed by Ophus et al.²⁸ to eliminate artefacts from beam scan jittering. The FRWRtools plugin for Gatan Digital Micrograph software were used for the following GPA analysis. Averaged fast-Fourier transforms were used as strain templates. The real-space resolution was set to 1.5 nm to achieve a relatively accurate measurement in reciprocal space.

STEM EDS measurements

Quantitative energy dispersive X-ray mapping (energy dispersive X-ray spectroscopy, EDS) was conducted on both the water-quenched samples and aged samples using a TitanX microscope with a quad EDS detector. No chemical segregation was observed; results are summarized in Extended Data Fig. 7. The lack of any visible chemical segregation via EDS analysis in the aged samples is consistent with the HRSTEM observation presented in Extended Data Fig. 2, where there is no obvious Z-contrast difference despite different degrees of local lattice distortion. Previous theoretical studies^{6,7} revealed that the SRO in the CrCoNi MEA is in the range of several nearest neighbour distances and that the driving force for the formation of SRO is to avoid certain types of bonding. Combined with the observation presented in the current study, we can conclude that it is not necessary for the SRO structure to possess a strong chemical segregation. Further verification using atomic-resolution EDS or electron energy loss spectroscopy (EELS) could provide valuable insights revealing the atomic structure of SRO clusters.

Dislocation analysis

TEM dislocation analysis was conducted on both the water-quenched and the aged samples after 6% compressive deformation. TEM observations were conducted on the Zeiss LIBRA 200MC (operating at 200 kV) at NCEM. Low-angle annular dark-field DC-STEM images^{45,46} for 'g·b' analysis of the partial dislocations and SFE measurements were acquired on the TEAM I microscope. To identify the Burgers vectors of the partial dislocations, g·b analysis was performed where the contrast from a dislocation is eliminated (or minimized) by using a diffraction condition normal to the Burgers vector such that g·b = 0. The measured partial dislocation separation was further calibrated by conducting a g(3g) weak-beam

dark-field imaging and calculating the actual partial separation from the observed values^{20,47,48}. The SFEs were calculated according to the following equation^{20,49,50}:

$$\text{SFE} = \frac{Gb_p^2}{8\pi d} \left(\frac{2-\nu}{1-\nu} \right) \left(1 - \frac{2\nu \cos(2\beta)}{2-\nu} \right) \quad (3)$$

where G is the shear modulus of the CrCoNi MEA (determined by the ultrasonic pulse-echo measurement), b_p is the magnitude of the Burgers vector of partial dislocations (-0.146 nm), d is the measured separation of partial dislocations, ν is Poisson's ratio (determined by the ultrasonic pulse-echo measurement), and β is the angle between the perfect dislocation Burgers vector and the dislocation line. For both the 1,000 °C aged samples and water-quenched samples, 50 individual measurements were conducted on more than 10 partial pairs from relatively thick regions to avoid any surface effects. Associated \pm standard deviations were calculated to ensure accurate and representative results.

Nanoindentation experiments

Nanoindentation tests were conducted on a Bruker Ti 950 TriboIndenter instrument with a 1- μ m Berkovich tip. The peak load was set to 1,000 μ N. The analysis was conducted with a calibrated area function of the tip. The water-quenched and 1,000 °C aged samples were electrochemically polished on one side with a solution of 70% methanol, 20% glycerol and 10% perchloric acid at -20 °C. A 10 \times 10 grid of indentations covering an area of 1 mm \times 1 mm was set to conduct the test for each sample. No strong texture was observed by post-test EBSD. All quantitative parameters were averaged over the 100 indentations with associated \pm standard deviations.

Bulk mechanical tests

Bulk tensile tests were carried out on an MTS Criterion (Model 43) system. A Sony A7R Mark II camera was used to record images for Digital Image Correlation (DIC). A copy of Vic-2D Image Correlation software was used to conduct the DIC analysis. Owing to the limited amount of material, the dimension of the gauge section of both water-quenched and 1,000 °C aged samples was set to 5.1 mm \times 0.8 mm \times 1.6 mm. Specially designed sample grippers were used to conduct the tensile test. Sample surfaces were mechanically polished and sparkle-sprayed before the tests. The strain was extracted from the DIC von Mises strain data using the 'virtual extensometers' mode and averaged three virtual extensometers along the gauge length.

Diffuse anti-phase boundary energy

The diffuse anti-phase boundary (DAPB) energy as a function of dislocation slip events was calculated via density functional theory using an 'aged' atomic model reported in previous literature⁶, which has an SFE similar to that of the 1,000 °C aged samples. Excess energy was calculated after each successive slip was introduced into the system.

Elastic modulus measurements

In addition to the effect of SRO on plastic behaviour, it also, in theory, should affect elastic properties as the local bonding environments are substantially altered from the perfect random solid solution. A simple rule-of-mixtures would predict a Young's modulus of ~229 GPa for equiatomic CrCoNi (ref. ³⁸). However, the nanoindentation modulus (reduced modulus) of the water-quenched sample is measured to be 181.76 \pm 13.37 GPa, 18.1% smaller than that of the 1,000 °C aged sample (214.79 \pm 18.49 GPa). In contrast, the global Young's modulus of the bulk materials was determined by the ultrasonic pulse-echo technique where the longitudinal and transverse sound speeds are measured to calculate elastic modulus. An Olympus 38DL Plus thickness gauge with a Model 5072PR pulser/receiver module was used to measure the

speed of the shear velocity and the longitudinal velocity. The Poisson's ratio, Young's modulus and the shear modulus were calculated with the following equations:

$$\nu = \frac{1 - 2(V_T/V_L)^2}{2 - 2(V_T/V_L)^2} \quad (4)$$

$$E = \frac{V_L^2 \rho (1 + \nu)(1 - 2\nu)}{1 - \nu} \quad (5)$$

$$G = V_T^2 \rho \quad (6)$$

where ν is the Poisson's ratio, V_T is the shear velocity, V_L is the longitudinal velocity, E is the Young's modulus, G is the shear modulus and ρ is the density of the materials, which is estimated with the following equation:

$$\rho = \frac{4m_{a\text{Avg}}}{V_{\text{cell}}} \quad (7)$$

where $m_{a\text{Avg}}$ is the averaged atomic mass of Cr, Co and Ni, V_{cell} is the volume of an fcc unit cell calculated with the lattice constants derived from the XRD results.

The measured global Young's modulus of the water-quenched and the aged samples was 229.93 GPa and 230.99 GPa, respectively (other measured elastic properties are listed in Extended Data Table 1). The discrepancy between the locally-measured modulus by nanoindentation and the bulk-scale modulus measured acoustically may result from the limited size (~1 nm) of SRO clusters. The local measurement of modulus by nanoindentation is sensitive to the homogeneity of the distribution of the SRO clusters. However, the wavelength of the ultrasonic acoustic waves used to measure global modulus is orders of magnitude longer than the size of the SRO. Therefore, the measurement is averaged over a much larger volume and is insensitive to the degree of SRO.

Data availability

The data that support the findings of this study are available from the corresponding author upon reasonable request.

44. Fultz, B. & Howe, J. M. *Transmission Electron Microscopy and Diffractometry of Materials* (Springer, 2008).
45. Phillips, P. J., Brandes, M. C., Mills, M. J. & de Graef, M. Diffraction contrast STEM of dislocations: imaging and simulations. *Ultramicroscopy* **111**, 1483–1487 (2011).
46. Phillips, P. J. et al. Atomic-resolution defect contrast in low angle annular dark-field STEM. *Ultramicroscopy* **116**, 47–55 (2012).
47. Cockayne, D. J. H. The weak-beam technique as applied to dissociation measurements. *J. Phys. Colloq.* **35**, C7-141–C7-148 (1974).
48. Cockayne, D. J. H., Ray, I. L. F. & Whelan, M. J. Investigations of dislocation strain fields using weak beams. *Phil. Mag.* **20**, 1265–1270 (1969).
49. Anderson, P. M., Hirth, J. P. & Lothe, J. *Theory of Dislocations* (Cambridge Univ. Press, 2017).
50. Pierce, D. T. et al. The influence of manganese content on the stacking fault and austenite/ ϵ -martensite interfacial energies in Fe–Mn–(Al–Si) steels investigated by experiment and theory. *Acta Mater.* **68**, 238–253 (2014).

Acknowledgements This work was primarily supported by the US Department of Energy, Office of Science, Office of Basic Energy Sciences, Materials Sciences and Engineering Division, under contract no. DE-AC02-05-CH11231 within the Damage-Tolerance in Structural Materials (KC 13) programme. R.Z., S.Z. and Y.C. acknowledge support from the US Office of Naval Research under grant nos. N00014-12-1-0413, N00014-17-1-2283 and N00014-11-1-0886, respectively. Work at the Molecular Foundry was supported by the Office of Science, Office of Basic Energy Sciences, of the US Department of Energy under contract no. DE-AC02-05CH11231. X-ray diffraction measurements were made at the Stanford Nano Shared Facilities (SNSF), supported by the National Science Foundation under award ECCS-1542152. This research used resources of the National Energy Research Scientific Computing Center (NERSC), a US Department of Energy Office of Science User Facility operated under contract no. DE-AC02-05CH11231. We thank E. Ma at Johns Hopkins University for providing a 600 °C aged alloy.

Article

Author contributions R.Z., S.Z., M.A., R.O.R. and A.M.M. conceived the project; R.Z. and S.Z. conducted the energy-filtered TEM imaging and dislocation analysis; C.O. and R.Z. developed and optimized the domain recognition algorithm; R.Z. and S.Z. conducted the nanoindentation tests; R.Z., S.Z. and Y.C. conducted the tensile tests. J.D. conducted the DFT simulations. T.J. conducted the XRD experiments. R.Z., S.Z., R.O.R., M.A. and A.M.M. prepared the manuscript, which was reviewed and edited by all authors. Project administration, supervision and funding acquisition was performed by R.O.R., M.A. and A.M.M.

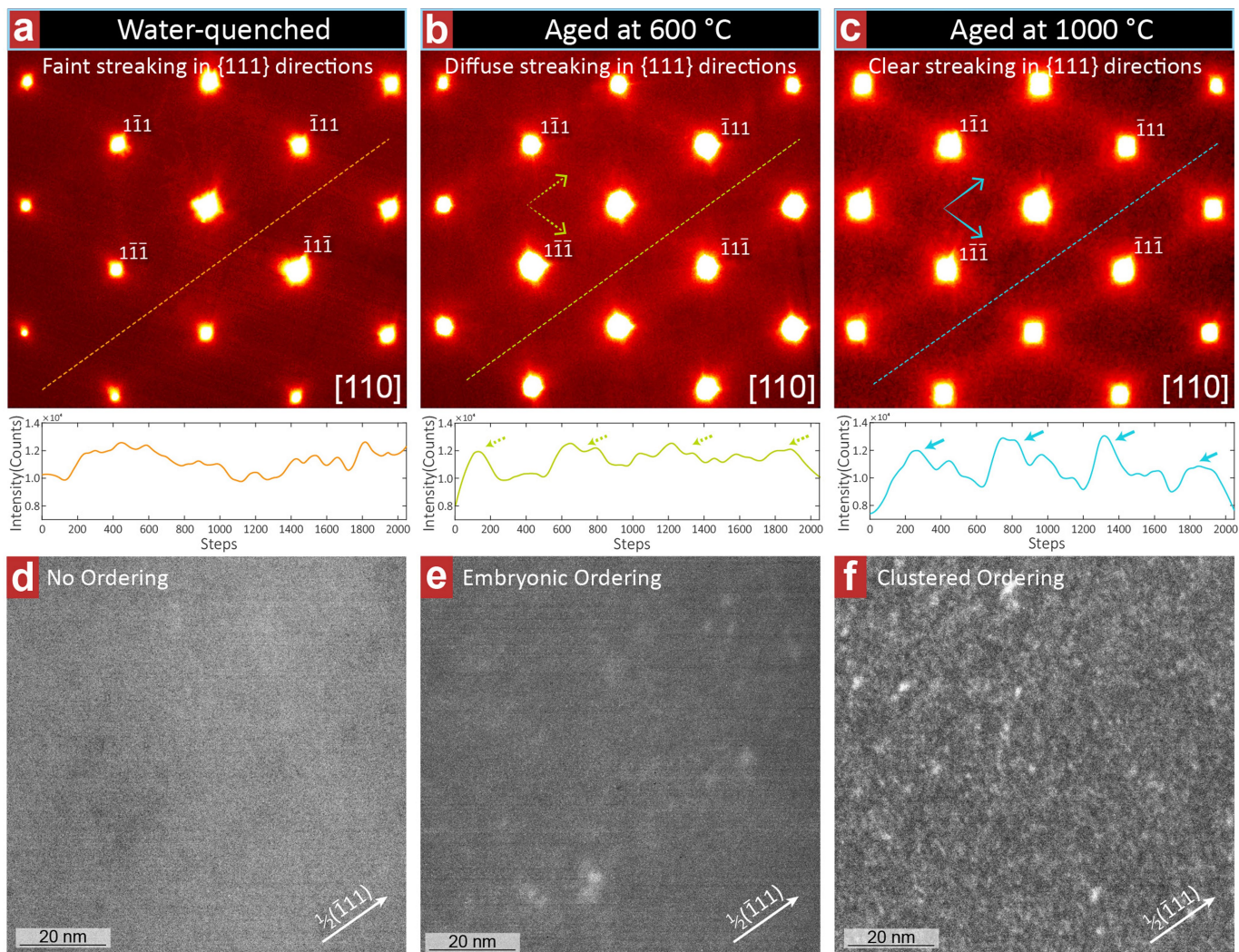
Competing interests The authors declare no competing interests.

Additional information

Correspondence and requests for materials should be addressed to A.M.M.

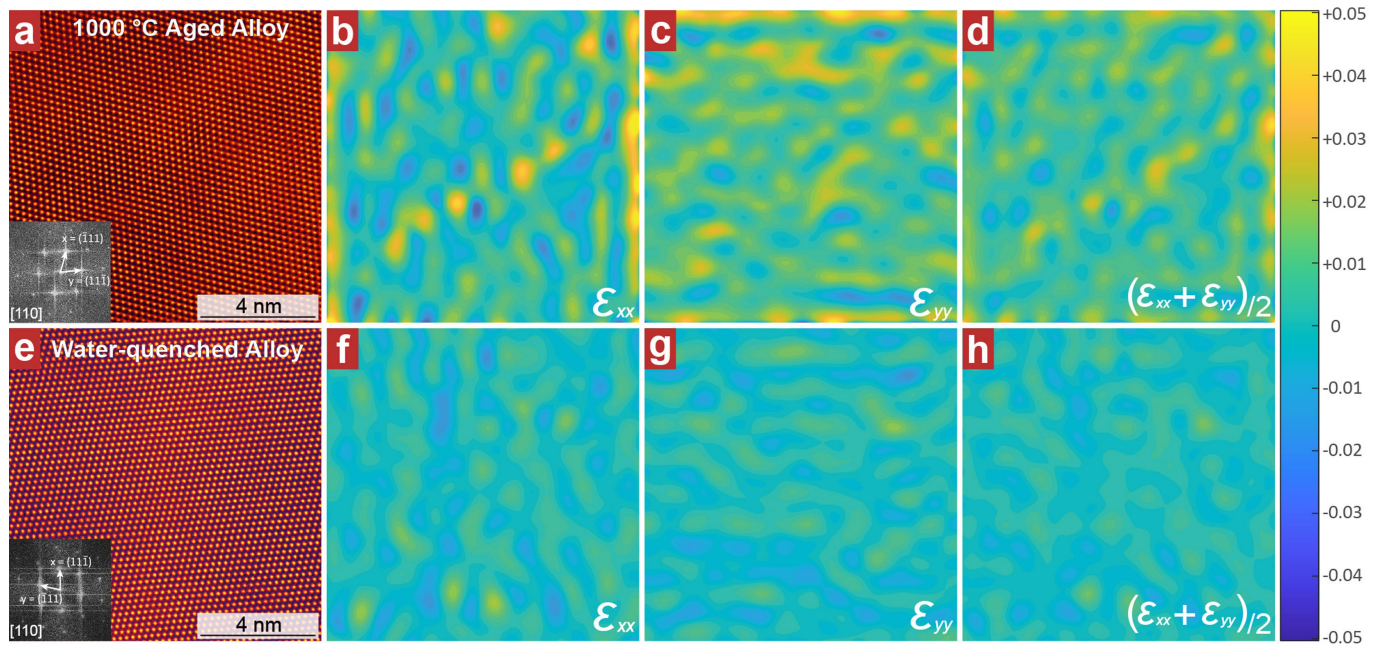
Peer review information *Nature* thanks Elena Pereloma, Christopher Woodward and the other, anonymous, reviewer(s) for their contribution to the peer review of this work.

Reprints and permissions information is available at <http://www.nature.com/reprints>.



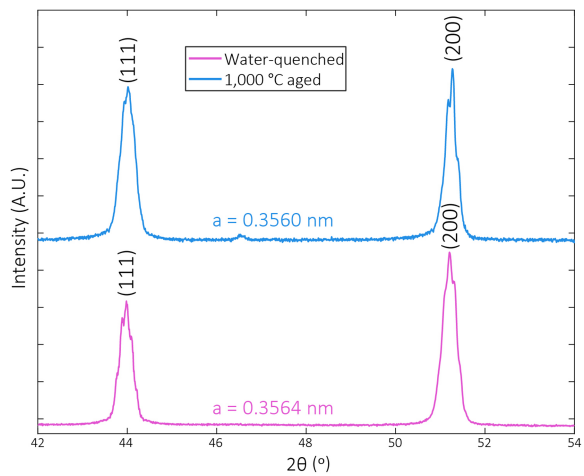
Extended Data Fig. 1 | Energy-filtered TEM diffraction patterns and dark-field images formed with diffuse superlattice streaks.
a–c, Energy-filtered diffraction patterns taken from CrCoNi MEA samples that were water-quenched, aged at 600 °C for one week or aged at 1,000 °C for one week, respectively. The contrast is pseudo-coloured for better visibility. The line plots of intensity show the periodic intensity of the diffuse superlattice

streaks. **d–f,** Energy-filtered dark-field images taken from water-quenched, 600 °C aged and 1,000 °C aged samples, respectively. The aperture positions are marked by the \mathbf{g} vectors (labelled arrows). The images of the water-quenched and the 1,000 °C aged samples are the same as in Fig. 1 but are presented again here for comparison with the 600 °C aged sample.



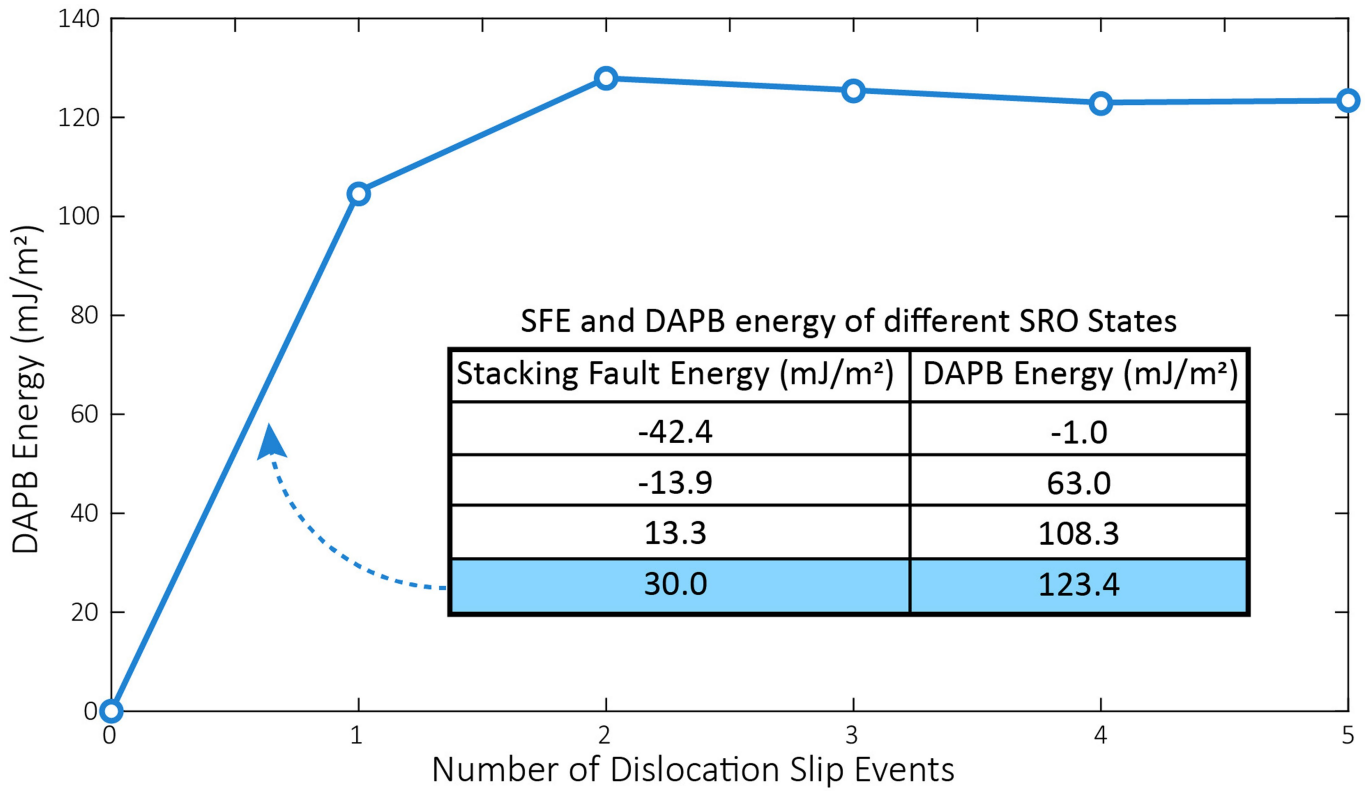
Extended Data Fig. 2 | Geometrical phase analysis strain mapping of a 1,000 °C aged sample and a water-quenched sample. a–d, 1,000 °C aged alloy; e–h, water-quenched sample. a, e, Drift-corrected HRSTEM images of the 1,000 °C aged sample and the water-quenched sample, respectively. The fast

Fourier transformed images are shown inset. **b–d, Strain maps of a** showing nanometre-sized local fluctuations of strain (ϵ_{xx} , normal strain in the x direction; ϵ_{yy} , normal strain in the y direction). **f–h, Strain maps of e** showing similar but much weaker contrast of local strain.

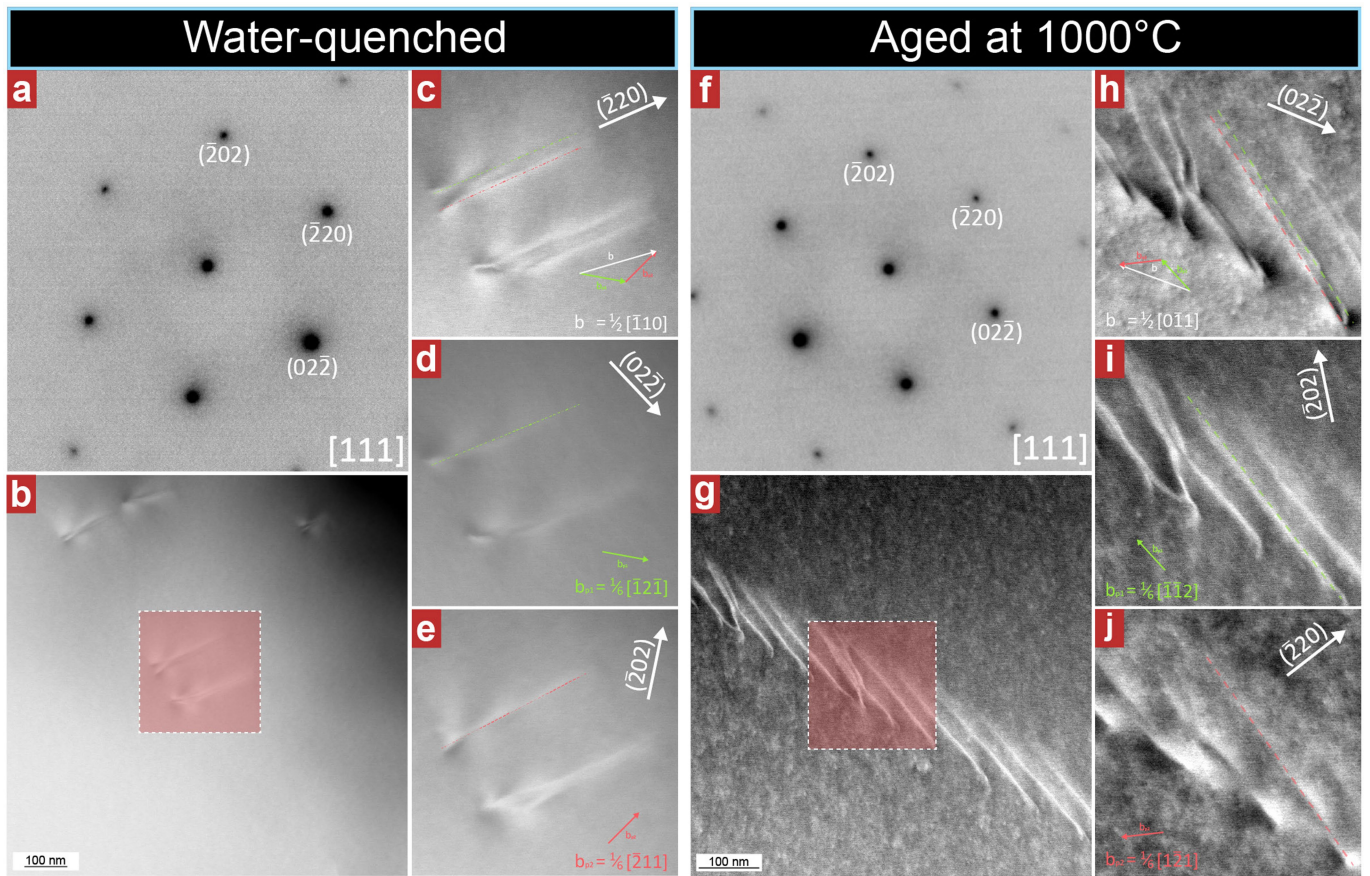


Extended Data Fig. 3 | Results of X-ray diffraction experiments on a water-quenched sample and a 1,000 °C aged sample of the CrCoNi MEA. The indexed (111) and (200) peaks are marked. The lattice constants a are calculated on the basis of the 2θ angles of the identified peaks.

Article



Extended Data Fig. 4 | Diffuse anti-phase boundary (DAPB) energy as a function of successive dislocation slip events from a calculated SRO model. The data in the inset table represent different states of SRO and the plot is from the state marked blue.

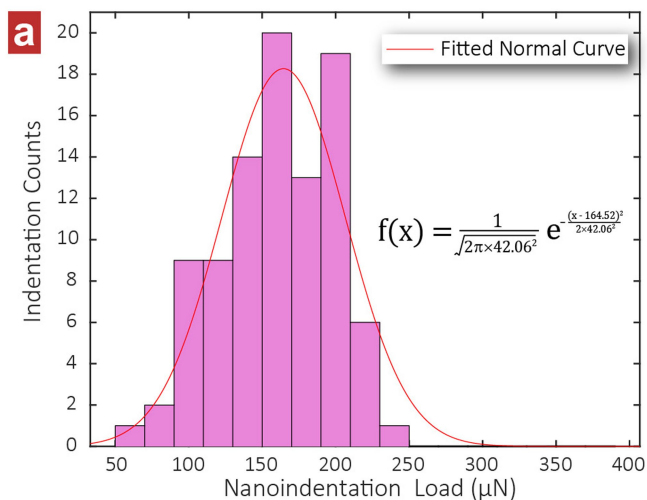


Extended Data Fig. 5 | Detailed 'g·b' analysis of partial dislocations in the CrCoNi MEA. **a–e**, Water-quenched sample; **f–j**, sample aged at 1,000 °C. **a, f**, Diffraction references showing the diffraction conditions (**g** vectors) used for the analysis. **b, g**, Lower-magnification DC-STEM images of dislocations in

the water-quenched and aged samples, respectively. **c–e, h–j**, Two-beam DC-STEM images of the boxed areas in **b** and **g**, respectively; the Burgers vectors of the visible dislocations are noted on the images.

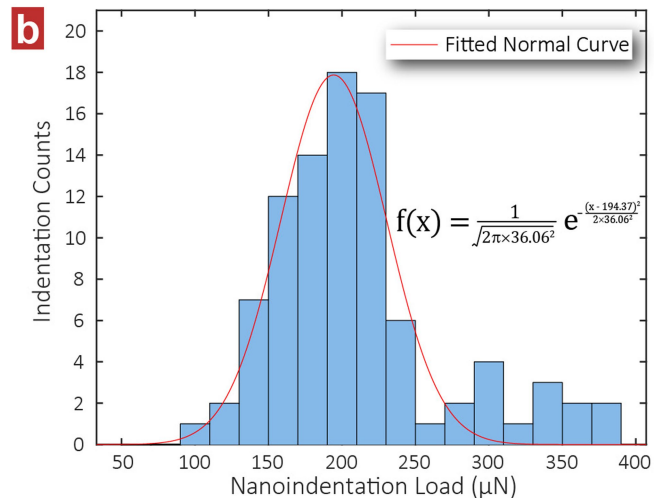
Water-quenched

Distribution of Pop-in Load

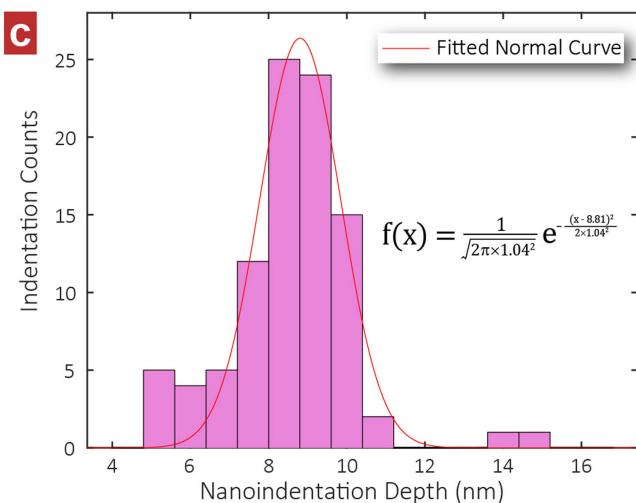


Aged at 1000 °C

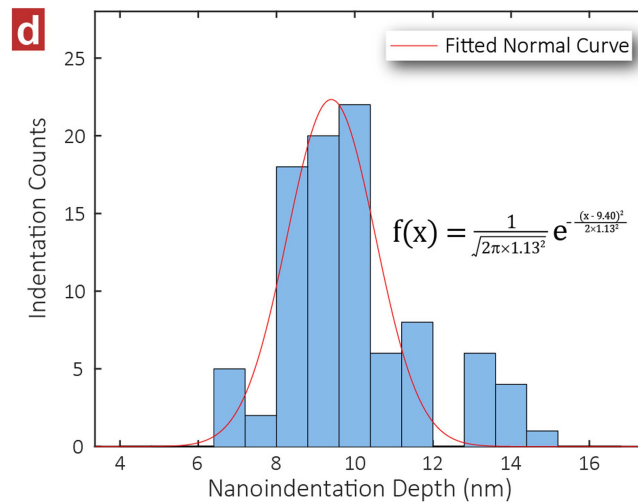
Distribution of Pop-in Load



Distribution of Pop-in Depth

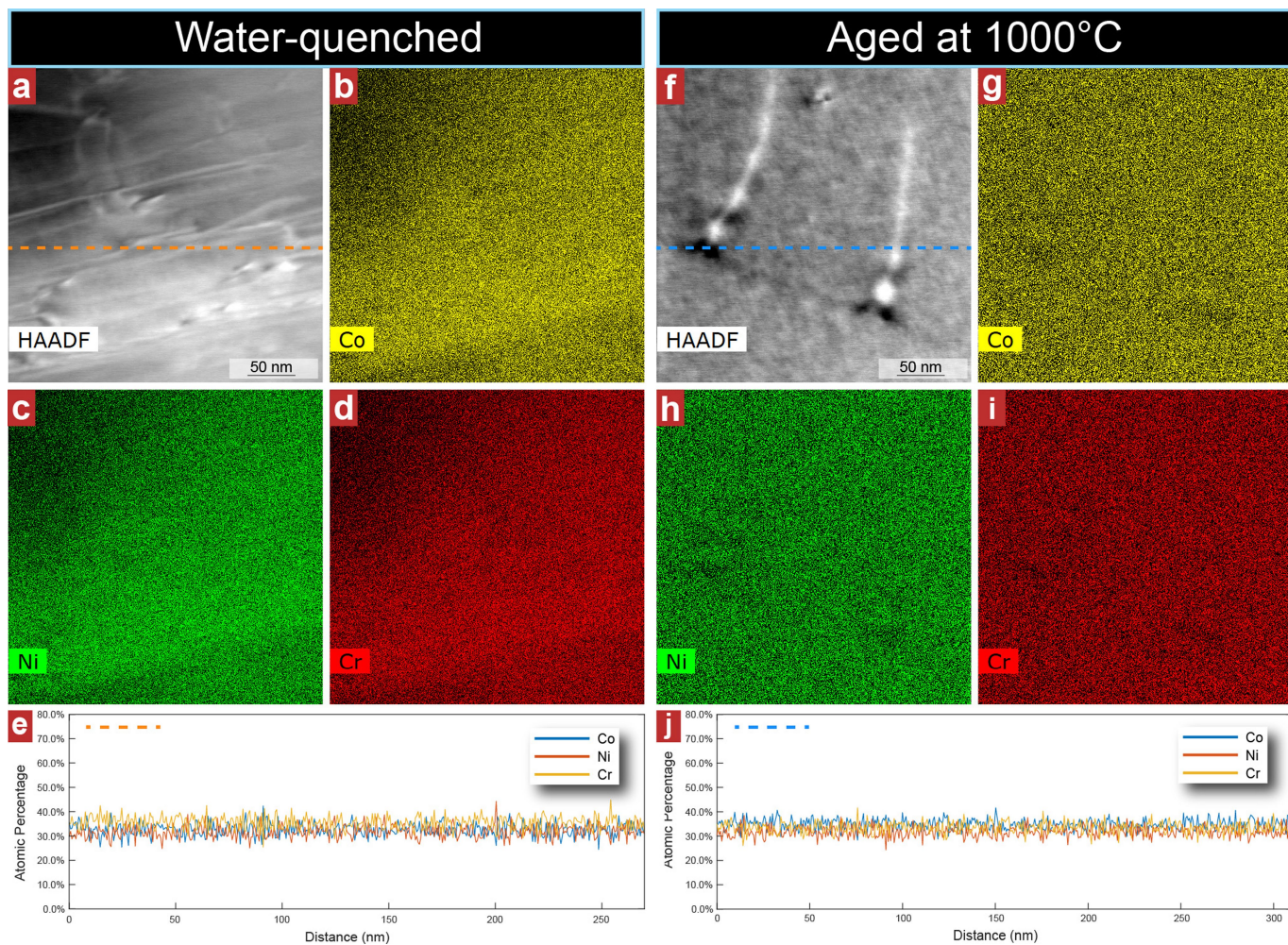


Distribution of Pop-in Depth



Extended Data Fig. 6 | Detailed statistical analysis of the pop-in events. Pop-in events were observed during nanoindentation tests (see Methods section 'Nanoindentation experiments' for details). **a, b**, Distribution of the pop-in load from water-quenched and 1,000 °C aged samples, respectively.

c, d, Distribution of the pop-in depth from water-quenched and 1,000 °C aged samples, respectively. The fitted normal distribution functions are listed in the panels. The results of numerical analysis are summarized in Extended Data Table 1.



Extended Data Fig. 7 | Element mapping of the water-quenched and aged CrCoNi samples using EDS. a–e, Water quenched sample; f–j, sample aged at 1,000 °C. a, f, Reference HAADF (high-angle annular dark field) images showing the regions of interest of a water-quenched sample and a 1,000 °C aged sample,

respectively. b–d, g–i, Element mapping of Co, Ni and Cr of the water-quenched sample and the 1,000 °C aged sample, respectively. e, j, Quantitative results of line scans of the water-quenched sample and the 1,000 °C aged sample, respectively. The line scan directions are marked by the dashed lines in a and f.

Article

Extended Data Table 1 | Statistical results of SFE measurements and nanoindentation tests

		Water-Quenched	Aged at 1000 °C
Elastic Properties	Poisson's Ratio	0.29	0.28
	Young's Modulus (GPa)	229.9	231.0
	Shear Modulus (GPa)	89.1	90.2
Yield Strength	0.2% Offset Yield Strength (MPa)	205	255
Dislocation Dissociation	Partial Separation, (nm)	13.59 ± 2.64	6.44 ± 1.19
	SFE (mJ/m ²)	8.18 ± 1.43	23.33 ± 4.31
Nanoindentation	Reduced Modulus (GPa)	181.76 ± 13.37	214.79 ± 18.49
	Indentation Hardness (GPa)	4.07 ± 0.23	4.37 ± 0.58
	Pop-in Load (μN)	164.52 ± 42.06	194.37 ± 36.06
	Pop-in Starting Displacement (nm)	8.81 ± 1.04	9.40 ± 1.13

Extended Data Table 2 | Detailed steps of the Gaussian template fitting process

Step	Description	Equation and comment
1	The standard deviation range of the Gaussian templates was set to 3 to 40 pixels (with a 0.1 interval) based on the pixel size of the DF image (0.056 nm/pixel).	
2	2-D Gaussian kernels with the same resolution as the DF images were constructed. The radius assumed for the SRO-enhanced domains was set to 1.3*sigma to best match the contrast observed in the DF image.	
3	To suppress the background noise during convolution, each Gaussian kernel was normalized by a larger Gaussian function to give a zero summation, using the expression at right, where G_{2D} is the normalized 2-D Gaussian template, σ is the varying standard deviation of the differently sized kernels, and x and y are the 2D coordinates from the kernel origin.	$G_{2D}(x, y, \sigma) = \frac{1}{2\pi\sigma^2} e^{-\frac{x^2+y^2}{2\sigma^2}} - \frac{1}{2\pi(1.5\sigma)^2} e^{-\frac{x^2+y^2}{2(1.5\sigma)^2}}$
4	The domain signals in the DF image were identified by a 2-D Gaussian Hough transform. For each kernel in the list, a 2-D convolution between the DF image and the kernel would be performed using the expression at right, where x is the DF image, h is the kernel and y is the result of the convolution.	$y[m, n] = \sum_j \sum_i x[i, j] \cdot h[m - i, n - j]$
5	After each convolution, pixels of the convolution result are compared to a data storing array; if the current pixel has a higher signal, the corresponding value would be updated in the data storing array. Another similarly sized array was used to store the associated kernel size of the highest signal.	
6	After the iterations, the pixel values were first filtered by the domain diameter range and the peak signal cutoff. Then the local peaks in the result array were identified if a pixel has a higher value than all of its eight neighbour pixels.	
7	The identified peaks were ordered and checked in a “brightest to dimmest” manner according to their pixel value. If dimmer peaks appear in the radius of a brighter peak, they would be deleted. This process is to eliminate overlapping entities.	
8	The remaining peaks were treated as identified domains.	
9	The diameter cutoff below 0.7 nm is set manually as this is already the size of the 1st nearest-neighbour shell of atoms in the MEA lattice, we do not regard anything below this value as an SRO domain.	

See Methods section ‘Energy-filtered TEM and SRO recognition’ for details.